DTU Library

IC 751: A New Changing Look AGN Discovered By NuSTAR

Ricci, C.; Bauer, F. E.; Arevalo, P.; Boggs, S.; Brandt, W. N.; Christensen, Finn Erland; Craig, W. W.; Gandhi, P.; Hailey, C. J.; Harrison, F. A.

Total number of authors:
15

[Link back to DTU Orbit](#)

IC 751: A NEW CHANGING LOOK AGN DISCOVERED BY *NUSTAR*

C. Ricci[1,2], F. E. Bauer[1,2,3,4], P. Arevalo[5], S. Boggs[6], W. N. Brandt[7,8,9], F. E. Christensen[10], W. W. Craig[6], P. Gandhi[11],
C. J. Hailey[12], F. A. Harrison[13], M. Koss[14], C. B. Markwardt[15,16], D. Stern[17], E. Treister[2,18], and W. W. Zhang[16]

[1] Instituto de Astrofísica, Facultad de Física, Pontificia Universidad Católica de Chile, Casilla 306, Santiago 22, Chile; cricci@astro.puc.cl
[2] EMBIGGEN Anillo, Concepción, Chile
[3] Millennium Institute of Astrophysics, Vicuña Mackenna 4860, 7820436 Macul, Santiago, Chile
[4] Space Science Institute, 4750 Walnut Street, Suite 205, Boulder, CO 80301, USA
[5] Instituto de Física y Astronomía, Facultad de Ciencias, Universidad de Valparaíso, Gran Bretana N 1111, Playa Ancha, Valparaíso, Chile.
[6] Space Sciences Laboratory, University of California, Berkeley, CA 94720, USA
[7] Department of Astronomy and Astrophysics, The Pennsylvania State University, University Park, PA 16802, USA
[8] Institute for Gravitation and the Cosmos, The Pennsylvania State University, University Park, PA 16802, USA
[9] Department of Physics, 104 Davey Lab, The Pennsylvania State University, University Park, PA 16802, USA
[10] DTU Space, National Space Institute, Technical University of Denmark, Elektronvej 327, DK-2800 Lyngby, Denmark
[11] School of Physics & Astronomy, University of Southampton, Highfield, Southampton SO17 1BJ, UK
[12] Columbia Astrophysics Laboratory, Columbia University, New York 10027, USA
[13] Cahill Center for Astronomy and Astrophysics, California Institute of Technology, Pasadena, CA 91125, USA
[14] Institute for Astronomy, Department of Physics, ETH Zurich, Wolfgang-Pauli-Strasse 27, CH-8093 Zurich, Switzerland
[15] Department of Astronomy, University of Maryland, College Park, MD 20742, USA
[16] Astroparticle Physics Laboratory, Mail Code 661, NASA Goddard Space Flight Center, Greenbelt, MD 20771, USA
[17] Jet Propulsion Laboratory, California Institute of Technology, Pasadena, CA 91109, USA
[18] Universidad de Concepción, Departamento de Astronomía, Casilla 160-C, Concepción, Chile

ABSTRACT

We present results of five *Nuclear Spectroscopic Telescope Array* (*NuSTAR*) observations of the type 2 active galactic nucleus (AGN) in IC 751, three of which were performed simultaneously with *XMM-Newton* or *Swift*/ X-Ray Telescope. We find that the nuclear X-ray source underwent a clear transition from a Compton-thick ($N_H \simeq 2 \times 10^{24}$ cm^{-2}) to a Compton-thin ($N_H \simeq 4 \times 10^{23}$ cm^{-2}) state on timescales of $\lesssim 3$ months, which makes IC 751 the first changing look AGN discovered by *NuSTAR*. Changes of the line of sight column density at the $\sim 2\sigma$ level are also found on a timescale of ~ 48 hr ($\Delta N_H \sim 10^{23}$ cm^{-2}). From the lack of spectral variability on timescales of ~ 100 ks, we infer that the varying absorber is located beyond the emission-weighted average radius of the broad-line region (BLR), and could therefore be related either to the external part of the BLR or a clumpy molecular torus. By adopting a physical torus X-ray spectral model, we are able to disentangle the column density of the non-varying absorber ($N_H \sim 3.8 \times 10^{23}$ cm^{-2}) from that of the varying clouds [$N_H \sim (1 - 150) \times 10^{22}$ cm^{-2}], and to constrain that of the material responsible for the reprocessed X-ray radiation ($N_H \sim 6 \times 10^{24}$ cm^{-2}). We find evidence of significant intrinsic X-ray variability, with the flux varying by a factor of five on timescales of a few months in the 2–10 and 10–50 keV band.

Key words: galaxies: active – galaxies: individual: (IC 751) – galaxies: Seyfert – X-rays: galaxies

1. INTRODUCTION

Variability of the line of sight column density (N_H) might be rather common in active galactic nuclei (AGNs; Risaliti et al. 2002; Bianchi et al. 2012; Torricelli-Ciamponi et al. 2014), and in the past decade several objects have been found to show eclipses of the X-ray source, both due to Compton-thick (CT; $N_H \gtrsim 10^{24}$ cm^{-2}) and to Compton-thin ($N_H < 10^{24}$ cm^{-2}) material. Since the X-ray source is believed to be located very close to the supermassive black hole (SMBH), this variable absorption could be associated either with broad-line region (BLR) clouds, or with clumps in the molecular torus. In at least a few cases (e.g., Risaliti et al. 2009; Maiolino et al. 2010) these variations have been found to occur on timescales of days, and are consistent with being related to material in the BLR. Markowitz et al. (2014) have recently shown, by studying *RXTE* light curves of 55 AGNs, that for eight objects of their sample there seems to be variation of absorbing material also on longer timescales (months to years). They associated these changes in N_H with clumps in the molecular torus. Interestingly, none of the eclipses detected by Markowitz et al. (2014) were due to CT material.

So far variations in the N_H of the neutral absorber have been found in more than 20 AGNs including 1H 0419−577 (Pounds et al. 2004), Centaurus A (Beckmann et al. 2011; Rivers et al. 2011), ESO 323−G77 (Miniutti et al. 2014), H0557−385 (Longinotti et al. 2009), MR 2251–178, Mrk 348, Mrk 509 (Markowitz et al. 2014), Mrk 6 (Immler et al. 2003), Mrk 766 (Risaliti et al. 2011), Mrk 79 (Markowitz et al. 2014), NGC 1068 (Marinucci et al. 2016), NGC 1365 (Risaliti et al. 2005, 2007; Maiolino et al. 2010; Walton et al. 2014; Rivers et al. 2015b), NGC 3227 (Lamer et al. 2003), NGC 3783 (Markowitz et al. 2014), NGC 4151 (Puccetti et al. 2007), NGC 4388 (Elvis et al. 2004), NGC 4395 (Nardini & Risaliti 2011), NGC 4507 (Braito et al. 2013; Marinucci et al. 2013), NGC 454 (Marchese et al. 2012), NGC 5506 (Markowitz et al. 2014), NGC 6300 (Guainazzi 2002), NGC 7582 (Piconcelli et al. 2007; Bianchi et al. 2009; Rivers et al. 2015a), NGC 7674 (Bianchi et al. 2005), PG 2112+059 (Gallagher et al. 2004), UGC 4203 (Guainazzi et al. 2002; Risaliti et al. 2010), and SWIFT J2127.4+5654 (Sanfrutos et al. 2013). In most cases these variations are due to Compton-thin material, and only for a handful of sources is the varying absorber CT (i.e., ESO 323−G77, NGC 1068, NGC 1365,

Table 1
X-Ray Observations Log

Obs. #	Facility	Observation Date	Observation ID	Net Exposure (ks)
1	*Swift*/XRT[a]	2008 Feb 20 13:13:01	00037374001	2.3
2	*NuSTAR*	2012 Oct 28 23:01:07	60061217002	13.1
3	*NuSTAR*	2013 Feb 04 00:26:07	60061217004	52.0
4	*NuSTAR*	2013 May 23 05:36:07	60061217006	25.0
4	*Swift*/XRT	2013 May 25 16:38:59	00080064001	5.8
5	*NuSTAR*	2014 Nov 28 06:01:07	60001148002	26.3
5	*XMM-Newton*	2014 Nov 28 13:20:42	0744040301	18.4[b]; 23.1[c]
6	*NuSTAR*	2014 Nov 30 06:26:07	60001148004	25.7
6	*XMM-Newton*	2014 Nov 30 13:11:46	0744040401	18.2[b]; 22.4[c]

Notes.
[a] This observation was not used for spectral fitting because of the low number of counts.
[b] EPIC/PN.
[c] EPIC MOS1 and MOS2.

NGC 454, NGC 6300, NGC 7582, NGC 7674, UGC 4203). AGNs switching between Compton-thin and CT states are usually called *changing look* AGNs (e.g., Matt et al. 2003) because their spectral shape changes dramatically (from transmission-dominated to reflection-dominated). In the optical band, changing look AGNs are objects that transition from type 1 to type 1.8/1.9/2 (e.g., LaMassa et al. 2015), or from type 1.8/1.9/2 to type 1 (e.g., Shappee et al. 2014). In the following, we will refer to the X-ray classification only.

IC 751 ($z = 0.0311$, $D = 137$ Mpc; Falco et al. 1999) is a type 2 AGN (Véron-Cetty & Véron 2010) in an edge-on spiral galaxy (de Vaucouleurs et al. 1991) that has not yet been studied in detail in the X-ray band. The source was reported in the 70 month *Swift*/Burst Alert Telescope (BAT) catalog (Baumgartner et al. 2013), and was observed by *Nuclear Spectroscopic Telescope Array* (*NuSTAR*) as part of the campaign aimed at following up on *Swift*/BAT-detected sources (M. Balokovic et al. 2016, in preparation). The interesting X-ray characteristics of this object triggered several follow-up observations with *NuSTAR*. We report here on the five *NuSTAR* observations of this source carried out between 2012 and 2014, two of which were performed jointly with *XMM-Newton*. The source switches from a CT to Compton-thin state between the different observations, and is the first changing look AGN discovered by *NuSTAR*. Following our X-ray spectral and temporal analysis, we put constraints on the location of the varying obscuring material. Throughout the paper, we consider a luminosity distance of the source of $d_L = 135$ Mpc, and adopt standard cosmological parameters ($H_0 = 70$ km s^{-1} Mpc^{-1}, $\Omega_m = 0.3$, $\Omega_\Lambda = 0.7$). Unless otherwise stated, all uncertainties are quoted at the 90% confidence level.

2. X-RAY OBSERVATIONS AND DATA REDUCTION

IC 751 was observed five times by *NuSTAR*, twice jointly with *XMM-Newton* (PI F. Bauer), and two times by the *Swift*/X-Ray Telescope (XRT). Details about these observations are reported in Table 1.

2.1. NuSTAR

NuSTAR (Harrison et al. 2013) is the first focusing X-ray telescope in orbit operating above 10 keV. *NuSTAR* consists of two focal-plane modules (FPMA and FPMB), both operating in the 3–79 keV band and with similar characteristics.

NuSTAR observed IC 751 five times between 2012 October and 2014 November, with exposure times ranging between 13 and 52 ks (Table 1). The data collected by *NuSTAR* were processed using the *NuSTAR* Data Analysis Software NUSTARDAS v1.4.1 within Heasoft v6.16, using the latest calibration files, released in 2015 March (Madsen et al. 2015). The source spectra and light curves were extracted using the NUPRODUCTS task, selecting circular regions with a radius of 50″. The background spectra and light curves were obtained in a similar fashion, using a circular region of 60″ radius located where no other source was detected. The source light curve was corrected for background using the LCMATH task.

2.2. XMM-Newton

The *XMM-Newton* X-ray observatory (Jansen et al. 2001) observed IC 751 twice at the end of 2014 November. We analyzed the two ∼20 ks *XMM-Newton* observations of IC 751, taking into account the data obtained by the PN (Strüder et al. 2001) and MOS (Turner et al. 2001) cameras. The observation data files (ODFs) were reduced using the the *XMM-Newton* Standard Analysis Software version 12.0.1 (Gabriel et al. 2004). The raw PN (MOS) data files were then processed using the EPCHAIN (EMCHAIN) task.

For both observations we analyzed the background light curves in the 10–12 keV band (EPIC/PN), and above 10 keV (EPIC/MOS), to filter the exposures for periods of high background activity. We set the threshold to 0.5 ct s^{-1} and to 0.3 ct s^{-1} for PN and MOS, respectively. This resulted in about 10% of the observations being filtered out. We report the final exposures used in Table 1. Only patterns that correspond to single and double events (PATTERN ⩽ 4) were selected for PN, and corresponding to single, double, triple, and quadruple events for MOS (PATTERN ⩽ 12).

For the three cameras, the source spectra were extracted from the final filtered event list using circular regions centered on the object, with a radius of 20″, while the background was estimated using circular regions with a radius of 40″ located on the same CCD as the source, where no other source was present. No pile up was detected for any of the three cameras in the two observations. The ARFs and RMFs were created using the ARFGEN and RMFGEN tasks, respectively. For both observations the source and background spectra of the two MOS cameras, together with the RMF and ARF files, were merged using the ADDASCASPEC task.

2.3. Swift

IC 751 was observed twice by the XRT (Burrows et al. 2005) on board the *Swift* observatory (Gehrels et al. 2004): for 2.3 ks in 2008 February and for 5.8 ks, two days after the *NuSTAR* observation, in 2013 May. During the first observation only five counts were detected, so that no detailed spectral analysis could be performed. The data were reduced using the XRTPIPELINE v0.13.0, which is part of the XRT Data Analysis Software within Heasoft v6.16.

The BAT on board *Swift* has been monitoring the sky in the 14–195 keV band since 2005, and has so far detected more than 800 AGNs (Baumgartner et al. 2013), 55 of which are CT sources (Ricci et al. 2015). Given the significant N_H variability of IC 751 found by *NuSTAR*, we did not use the 70 month stacked *Swift*/BAT spectrum for our spectral analysis. The long-term variability inferred by *Swift*/BAT will be discussed in Section 5. The 70 month averaged flux of IC 751 in the 14–195 keV band is $13.1^{+3.9}_{-3.6} \times 10^{-12}$ erg s^{-1} cm^{-2} (90% confidence interval).

3. X-RAY SPECTRAL ANALYSIS—SLAB MODEL

We performed X-ray spectral analysis with XSPEC v.12.8.2 (Arnaud 1996). To all models we added a photoelectric absorption component (TBABS; Wilms et al. 2000) to take into account Galactic absorption in the direction of the source, fixing the value of the column density to $N_H^G = 1.2 \times 10^{20}$ cm^{-2} (Kalberla et al. 2005). In order to use χ^2 statistics, *NuSTAR* FPMA/FPMB and *XMM-Newton* EPIC PN and MOS spectra were binned to have at least 20 counts per bin. Quoted errors correspond to a 90% confidence level ($\Delta\chi^2 = 2.7$). Given the low signal-to-noise of the *Swift*/XRT spectrum of Observation 4, we did not bin the spectrum, and applied Cash statistics (Cash 1979; CSTAT in XSPEC).

As a first step to shed light on the spectral variability, we used a model which considers reprocessed radiation from a slab to reproduce the X-ray spectrum of IC 751. Since the first two data sets lacked simultaneous coverage below 5 keV, and the *Swift*/XRT observation in Observation 4 did not have a very high signal-to-noise ratio, we used the two joint *NuSTAR*/*XMM-Newton* spectra (Observations 5 and 6, Section 3.1) to constrain the fundamental parameters (photon index, normalization of the reflection component, normalization of the Fe Kα line), and then used this information to fit the other observations (Observations 2, 3, and 4, Section 3.2), in order to constrain the value of the line of sight column density, N_H, and the normalization of the X-ray primary emission. Observation 1 was not used due to its poor statistics. It was, however, possible to infer the 2–10 keV flux of the X-ray source during this observation ($3.1^{+0.4}_{-2.4} \times 10^{-13}$ erg s cm^{-2}), which is consistent with that of Observation 3.

3.1. Observations 5 and 6

The slab model we used to analyze the broadband X-ray spectrum of IC 751 includes: (i) a power law with a high-energy cutoff, which represents the primary X-ray emission; (ii) photoelectric absorption and Compton scattering, to take into account the line of sight obscuration; (iii) unabsorbed X-ray reprocessed radiation; (iv) a Gaussian line to reproduce the Fe Kα emission; (v) a cutoff power-law component to reproduce the scattered X-ray emission; (vi) a thermal plasma model, to take into account a possible contribution of the host

galaxy to the X-ray spectrum below ∼2 keV. It must be stressed that the emission below 2 keV, which cannot be accounted for by the scattered component alone, could also be due to the blending of emission lines created by photo-ionization. However, due to the limited energy resolution of our data, in the following we will use a thermal plasma model. To reproduce photoelectric absorption and Compton scattering, we used the TBABS and CABS models, respectively. We took into account the reprocessed X-ray radiation using the PEXRAV model (Magdziarz & Zdziarski 1995), which assumes reflection from a semi-infinite slab. The value of the reflection parameter (R) was set to be negative in order to include only the reprocessed component. The values of the photon index (Γ), cutoff energy (E_C), and the normalization were fixed to the values of the cutoff power law, while the inclination angle of the observer with respect to the reflecting slab was set to $i = 30°$. This angle was selected considering the type 2 nature of IC 751, and assuming that the reflecting material is associated with the molecular torus. The width of the Fe Kα line (σ) was fixed to 40 eV, a value well below the energy resolution of *XMM-Newton* and *NuSTAR*, while the energy and normalization of the line were left free to vary. The width of the Fe Kα was chosen considering that the bulk of the line is created in material located in the BLR or in the molecular torus (e.g., Shu et al. 2010; Ricci et al. 2014a, 2014b). The scattered X-ray emission was taken into account by multiplying an additional unabsorbed cut off power law by a constant (f_{scatt}, typically of the order of a few percent), fixing all the parameters to those of the primary X-ray emission. A multiplicative constant to include possible cross-calibration offset between the different instruments was added, and was found to be typically $\lesssim 12\%$ of unity. In XSPEC our model is:

CONSTANT × TBABS$_{GAL}$ × [ZTBABS × CABS × CUTOFFPL + APEC + PEXRAV + ZGAUSS + f_{SCATT} × CUTOFFPL].

The results of the spectral fitting are reported in Table 2. In both Observations 5 and 6 we found the source in a Compton-thin state, with a photon index of $\Gamma \sim 1.9$ and a high-energy cutoff of $E_c \gtrsim 200$ keV. The two observations show a change in N_H (Figure 2), with Observation 5 being less obscured than Observation 6 ($\Delta N_H \sim 10^{23}$ cm^{-2}, significant at a ∼2σ level). The two observations also show evidence of intrinsic flux variation, with the source being significantly brighter in Observation 5. The reflection component appears to be rather weak, with a value of $R = 0.14^{+0.16}_{-0.13}$ in Observation 6, while it is less constrained in Observation 5 due to the higher flux level. The fraction of scattered flux is found to be $f_{scatt} \sim 0.5\%$ of the primary X-ray flux. The X-ray spectra and the ratio between the data and the best-fitting model are shown in Figure 1.

3.2. Observation 2, 3, and 4

To study Observations 2, 3, and 4, we set all the parameters, with the exception of the normalization of the primary X-ray emission and the column density, to the values obtained from the study of Observation 6. The normalization and N_H were allowed to vary within the uncertainties of the values obtained by fitting the X-ray spectrum of Observation 6. Observation 6 was chosen because the X-ray source was caught in a low-flux state, which allows better constraints on the normalization of the Fe Kα line and of the reprocessed X-ray emission.

Fitting Observation 2 with the approach described above, we obtained a chi-squared of 49.5 for 28 degrees of freedom (dof), and a clear excess below 6 keV. This excess can be removed by

Table 2
X-Ray Spectral Analysis—Slab Model

(1) Model Parameters	(2) Obs. 2 (2012 Oct 28)	(3) Obs. 3 (2013 Feb 04)	(4) Obs. 4 (2013 May 23)	(5) Obs. 5 (2014 Nov 28)	(6) Obs. 6 (2014 Nov 30)
Photon index Γ	1.96^{a}	1.74^{a}	1.73^{a}	$1.93^{+0.13}_{-0.12}$	$1.89^{+0.17}_{-0.17}$
Cutoff energy E_C (keV)	$\geqslant 222^{a}$	$\geqslant 222^{a}$	$\geqslant 222^{a}$	$\geqslant 192$	$\geqslant 222$
Reflection param. R	0.02^{a}	0.27^{a}	0.28^{a}	$\leqslant 0.17$	$0.14^{+0.16}_{-0.13}$
Col. density N_H (10^{22} cm^{-2})	199^{+75}_{-67}	121^{+29}_{-27}	32^{+9}_{-6}	38^{+3}_{-3}	49^{+7}_{-6}
Fraction of scattered component f_{scatt} (%)	$17.3^{+9.0}_{-10.5}$	0.9^{a}	0.9^{a}	$0.5^{+0.2}_{-0.2}$	$0.6^{+0.3}_{-0.2}$
Temperature kT (keV)	0.94^{b}	0.94^{b}	1.01^{a}	$0.82^{+0.15}_{-0.09}$	$0.94^{+0.07}_{-0.19}$
Energy (Fe Kα) (keV)	6.25^{a}	6.36^{a}	6.25^{a}	$6.42^{+0.08}_{-0.09}$	$6.36^{+0.10}_{-0.11}$
Norm. (Fe Kα) (10^{-6} photons cm^{-2} s^{-1})	2.1^{a}	1.9^{a}	1.5^{a}	$1.4^{+1.1}_{-1.0}$	$1.3^{+0.7}_{-0.8}$
EW(Fe Kα) (eV)	281^{+43}_{-218}	489^{+955}_{-26}	130^{+617}_{-65}	60^{+33}_{-44}	108^{+64}_{-39}
F^{obs}_{2-10} (10^{-12} erg cm^{-2} s^{-1})	$0.7^{+0.1}_{-0.5}$	$0.22^{+0.01}_{-0.08}$	$0.62^{+0.07}_{-0.06}$	$1.11^{+0.07}_{-0.12}$	$0.56^{+0.03}_{-0.09}$
F_{2-10} (10^{-12} erg cm^{-2} s^{-1})	22^{+3}_{-15}	$3.4^{+0.2}_{-1.2}$	$2.1^{+0.1}_{-0.2}$	$5.9^{+0.4}_{-0.6}$	$3.8^{+0.2}_{-0.6}$
F^{obs}_{10-50} (10^{-12} erg cm^{-2} s^{-1})	$4.2^{+0.5}_{-2.4}$	$3.5^{+0.1}_{-1.6}$	$3.9^{+0.3}_{-0.3}$	$5.2^{+0.3}_{-0.6}$	$3.5^{+0.2}_{-0.7}$
F_{10-50} (10^{-12} erg cm^{-2} s^{-1})	22^{+3}_{-13}	$6.7^{+0.2}_{-3.1}$	$4.7^{+0.4}_{-0.4}$	$7.3^{+0.4}_{-0.8}$	$5.2^{+0.3}_{-1.0}$
$\log L_{2-10}$ (erg s^{-1})	43.7	42.9	42.7	43.1	42.9
$\log L_{10-50}$ (erg s^{-1})	43.7	43.2	43.0	43.2	43.1
χ^2/dof	31.3/27	84.7/95	$131.9/111^{c}$	256.8/257	224.8/176

Notes. The table reports the model parameters obtained by fitting the X-ray spectra of the five epochs with the slab model: CONSTANT×TBABS_GAL×[ZTBABS×CABS×CUTOFFPL + APEC + PEXRAV + ZGAUSS + CONSTANT×CUTOFFPL] in XSPEC; the luminosities reported here are the intrinsic (i.e., absorption-corrected) values. For details see Section 3.1.
[a] Value of the parameter left free to vary within the uncertainties of Observation 6.
[b] Value of the parameter fixed.
[c] Poissonian statistics applied for *Swift*/XRT dta. The uncertainties reported for the Fe Kα EW correspond to the 68% confidence interval.

allowing the obscuring material to partially cover the X-ray source, so that some of the primary X-ray flux is able to leak out unabsorbed; i.e., by leaving f_{scatt} free to vary. This model yields a good value of chi-squared (χ^2/dof = 31.3/27), and a fraction of unabsorbed flux of ~17%. Assuming that the scattered fraction is ~0.5%, as found by the spectral analysis of Observations 5 and 6, this would imply that the absorber is covering ~83% of the X-ray source in the line of sight. The column density is significantly larger than in Observations 5 and 6, with the obscurer consistent with being CT [$\log(N_H/\text{cm}^{-2}) = 24.3$], while the source is in a high-flux state during this observation (Table 2).

The X-ray spectrum of Observation 3 shows that the X-ray source was also obscured by CT material ~3 months later [$\log(N_H/\text{cm}^{-2}) \sim 24.13$]. As can be seen in Figure 1, the source was no longer in a high-flux state, and the spectrum shows a prominent Fe Kα line (EW ~ 500 eV). Leaving the value of f_{scatt} free to vary does not significantly improve the chi-squared ($\Delta\chi^2 \sim 1$ for 1 less dof). The Fe Kα EW is higher in Observation 3 than in Observation 2 due to the higher flux level of the X-ray source during Observation 2.

The broadband *Swift*/XRT–*NuSTAR* spectrum of Observation 4 shows that IC 751 was in a Compton-thin state at the end of 2013 May, while the X-ray source was significantly dimmer with respect to the previous two observations, with its intrinsic flux level comparable to that observed during Observation 6.

4. X-RAY SPECTRAL ANALYSIS—TORUS MODEL

To further investigate the structure of the absorbers, and to disentangle the torus absorption from that caused by clouds in

the line of sight, assuming an homogeneous torus, we used the MYTORUS model[19] (Murphy & Yaqoob 2009). The MYTORUS model considers absorbed and reprocessed X-ray emission from a smooth torus with a half-opening angle θ_{OA} of 60°, and can be used for spectral fitting as a combination of three additive and exponential table models. These tabulated models include the zeroth-order continuum[20] (MYTORUSZ), the scattered continuum (MYTORUSS), and a component which contains the fluorescent emission lines (MYTORUSL).

4.1. Standard MYTorus

The analysis we carried out using the slab model (Section 3) showed that N_H is highly variable, so that it cannot be associated with a smooth absorber alone. This is also confirmed by the fact that applying the smooth MYTORUS model to all the X-ray spectra available, setting the values to be the same for the different observations, results in a chi-squared of $\chi^2 = 2628.2$ for 707 dof. Also considering different normalizations of the direct and scattered component or different values of the column density of the scattering and absorbing material fails to reproduce the X-ray spectrum, resulting in values of the reduced chi-squared of $\chi^2_\nu > 2$. We therefore used an alternative approach to take into account variable absorption by combining the non-varying torus absorption [MYTORUSZ (Tor)] with what we define as the *cloud absorption*. The geometry of the absorber we assume is shown in Figure 3. We adopted a model which includes the three components of MYTORUS plus a collisionally ionized plasma, and power law to reproduce the scattered component, similar to what was done

---

[19] http://www.mytorus.com/

[20] This component takes into account both Compton scattering and photoelectric absorption.
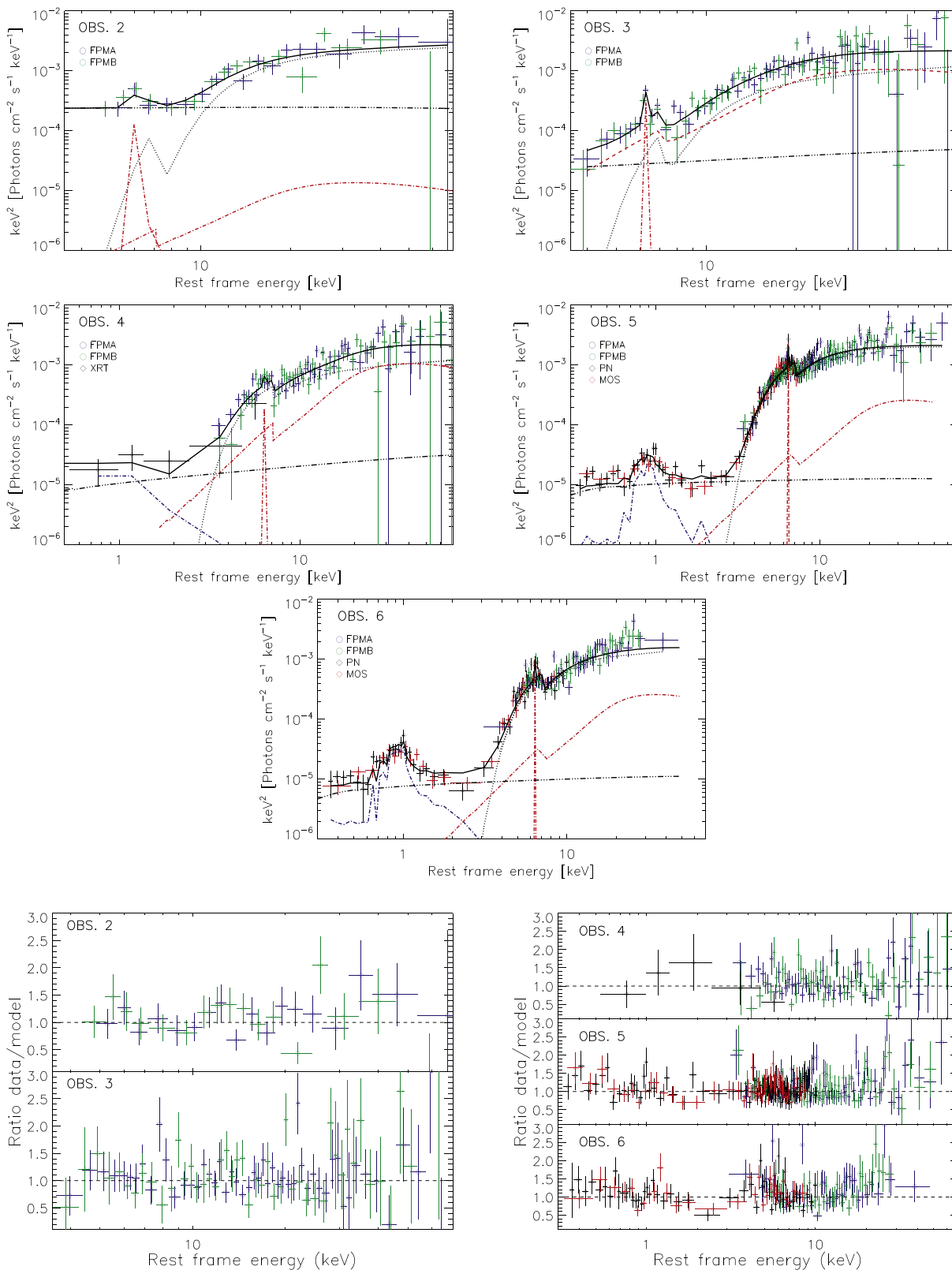
Figure 1. X-ray spectra of IC 751 obtained for the five observations discussed here. *Swift*/XRT data were rebinned to have a significance of at least 2σ per bin only for visual clarity. The black continuous line represents the best fit to the data obtained using the slab model described in Section 3.1. The black dotted line represents the absorbed primary cutoff power-law continuum, the red dotted–dashed line shows the features arising from reprocessed X-ray emission (Compton hump and Fe Kα line), the blue dotted–dashed line represents the collisionally ionized plasma emission, while the dotted–dotted–dashed black line is the scattered component. The bottom panels show the ratio between the data and the model obtained for the five observations (symbols are the same as for the X-ray spectra).
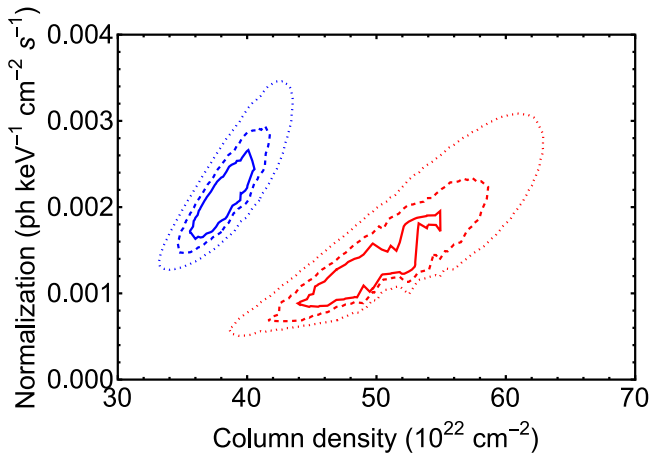
Figure 2. Contour plot of the power-law normalization and the column density for Observations 5 (blue) and 6 (red). Continuous, dashed, and dotted contours represent the 68%, 90%, and 99% confidence intervals, respectively.
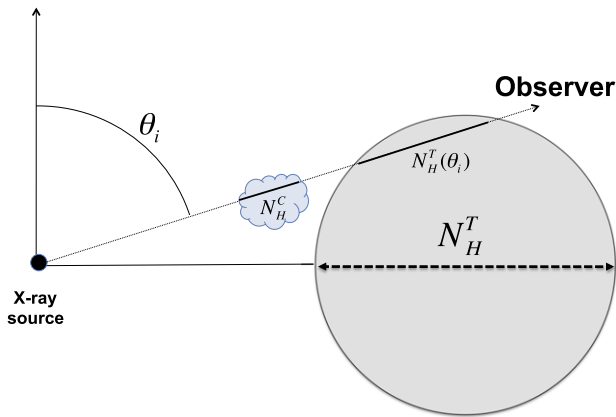
Figure 3. Geometry assumed for the torus model reported in Section 4.1. The parameters θ_i, N_H^C, $N_H^T(\theta_i)$, and N_H^T are the inclination angle, the column density of the cloud (variable), the column density of the torus at an angle θ_i (non-variable), and the equatorial (i.e., maximum) column density of the torus, respectively.

in Section 3. In order to take into account the variable absorber, we used an additional obscuring multiplicative component [MYTORUSZ(CLOUD, N_H^C)], where N_H^C is the column density of the cloud. In XSPEC the syntax of our model is:

CONSTANT×TBABS$_{GAL}$ × [MYTORUSZ(CLOUD) × MYTORUSZ (TOR) × ZPOWERLAW + MYTORUSS + APEC + GSMOOTH(MYTORUSL) +f_{scatt} × ZPOWERLAW].

The free parameters of MYTORUS are the photon index Γ, the equatorial column density of the torus N_H^T, and the inclination angle of the observer θ_i. We convolved the fluorescent emission lines of MYTORUS using a Gaussian function (GSMOOTH in XSPEC) to take into account the expected velocity broadening. We fixed the width of the lines to a FWHM of 2000 km s^{-1}, consistent with the average value obtained for 36 AGNs at $z < 0.3$ by the *Chandra*/HEG study of Shu et al. (2010). The model was also multiplied by a constant to take into account cross-calibration between the different spectra.

We simultaneously fitted the five sets of observations discussed above. The values of θ_i, N_H^T, Γ, and the normalization of the scattered component (n_{refl}, which includes the Compton hump) were left free to vary, and tied to be constant

for all observations. The normalization of the fluorescent lines was fixed to n_{refl}. The normalization of the primary power-law component (n_{po}), the value of N_H^C, and that of f_{scatt} were left free to have independent values for different observations.

The results obtained by this torus model are reported in the upper part of Table 3. The fit yields a chi-squared of $\chi^2 = 774.8$ (for 688 dof), and the primary X-ray emission has a value of the photon index consistent with that found using the slab model. As with the slab model, we find a clear variation of the line of sight column density, with the clouds having values of the column density spanning between 1.5×10^{24} and 5×10^{21} cm^{-2}. This approach also confirms a significant change in the value of f_{scatt} between the five observations, which varies between $\sim$4% and $\sim$0.4%. These variations in f_{scatt} are interpreted as being due to a partially covering absorber in the line of sight. Contrary to what we obtained using the slab model, applying MYTORUS we do not find a significant variation of the line of sight column density between Observation 5 and Observation 6. The model used, with the parameters set to those obtained for Observation 2, is shown in Figure 4.

We found an equatorial column density of N_H^T $\simeq 4.8 \times 10^{24}$ cm^{-2} and an inclination angle of the observer of $\theta_i \simeq 60°.3$, close to grazing incidence. The line of sight column density in the toroidal geometry assumed by MYTORUS can be obtained by

$$N_H^T(\theta_i) = N_H^T(1 - 4\cos^2\theta_i)^{\frac{1}{2}}, \qquad (1)$$

which implies that for IC 751 $N_H^T(\theta_i) \simeq 6.4 \times 10^{23}$ cm^{-2}, a value larger than the lowest column density inferred by adopting the slab model. However, given the dependence of the column density on the inclination angle, and the problems associated with the toroidal geometry for inclination angles close to the edges (see discussion in Yaqoob 2012), the uncertainty associated with this value is large.

4.2. Decoupled MYTorus

To further test the structure of the absorber, we applied MYTORUS in the *decoupled* mode (Yaqoob 2012). This was done by: (i) separating the column density of the absorbing [$N_H^T(Z)$] and reprocessing [$N_H^T(S, L)$] material, leaving both of them free to vary; (ii) fixing the inclination angle of MYTORUSL and MYTORUSS to $\theta_i(S, L) = 0°$, and that of MYTORUSZ to $\theta_i(Z) = 90°$; (iii) adding a second scattered component with $\theta_i(S, L) = 90°$ and the same column density and normalization of the one with $\theta_i(S, L) = 0°$; (iv) leaving the normalizations of the two components (n_{po} and n_{refl}) free, as was done in Section 4.1. The model we used assumes a geometry which consists of two absorbers, one varying and one constant with time, plus reprocessing material with a different value of the column density.

The results obtained are reported in the lower part of Table 3. The decoupled MYTORUS model yields a better chi-squared ($\chi^2 = 749.2$) than the non-decoupled one, for the same number of dof. The values of f_{scatt} are consistent with those found by applying the standard MYTORUS model, while the power-law continuum is slightly steeper. With this model we find a significant variation of N_H^C between Observations 5 and 6, similar to what we found using PEXRAV.

Table 3
X-Ray Spectral Analysis—Torus Model

				MYTorus				
(1) Observation	(2) N_H^C (10^{22} cm^{-2})	(3) n_{po} (10^{-3} ph keV^{-1} cm^{-2} s^{-1})	(4) Γ	(5) N_H^T (10^{24} cm^{-2})	(6) θ_i (deg)	(7) n_{refl} (10^{-3} ph keV^{-1} cm^{-2} s^{-1})	(8) kT (keV)	(9) f_{scatt} (%)
2 [2012.82]	150^{+19}_{-15}	$3.83^{+0.43}_{-0.42}$	$1.88^{+0.01}_{-0.04}$	$4.76^{+0.09}_{-0.27}$	$60.3^{+0.2}_{-0.2}$	$1.14^{+0.15}_{-0.11}$	$0.93^{+0.04}_{-0.04}$	$4.2^{+0.8}_{-0.8}$
3 [2013.10]	111^{+8}_{-7}	$2.10^{+0.18}_{-0.17}$	//	//	//	//	//	$1.6^{+0.5}_{-0.5}$
4 [2013.39]	$5.1^{+3.0}_{-3.1}$	$0.94^{+0.06}_{-0.06}$	//	//	//	//	//	$3.2^{+1.5}_{-1.2}$
5 [2014.91]	$0.58^{+0.08}_{-0.05}$	$1.83^{+0.07}_{-0.05}$	//	//	//	//	//	$0.4^{+0.1}_{-0.1}$
6 [2014.92]	$0.49^{+0.10}_{-0.05}$	$0.75^{+0.04}_{-0.04}$	//	//	//	//	//	$0.8^{+0.1}_{-0.1}$
				MYTorus—Decoupled Mode				
Observation	N_H^C (10^{22} cm^{-2})	n_{po} (10^{-3} ph keV^{-1} cm^{-2} s^{-1})	Γ	$N_H^T(Z)$ (10^{24} cm^{-2})	$N_H^T(S,L)$ (10^{24} cm^{-2})	n_{refl} (10^{-3} ph keV^{-1} cm^{-2} s^{-1})	kT (keV)	f_{scatt} (%)
2 [2012.82]	147^{+82}_{-48}	$4.71^{+6.29}_{-2.45}$	$1.98^{+0.08}_{-0.07}$	$0.37^{+0.02}_{-0.02}$	$6.0^{+3.5}_{-2.2}$	$1.22^{+0.50}_{-0.36}$	$0.93^{+0.05}_{-0.11}$	$4.1^{+3.4}_{-2.0}$
3 [2013.10]	105^{+32}_{-26}	$2.43^{+1.60}_{-0.90}$	//	//	//	//	//	$1.6^{+0.9}_{-0.7}$
4 [2013.39]	$\leqslant 18$	$1.20^{+0.45}_{-0.30}$	//	//	//	//	//	$2.7^{+3.4}_{-1.8}$
5 [2014.91]	$0.64^{+0.17}_{-0.07}$	$2.08^{+0.05}_{-0.03}$	//	//	//	//	//	$0.4^{+0.1}_{-0.1}$
6 [2014.92]	$11.1^{+5.0}_{-4.9}$	$1.28^{+0.38}_{-0.27}$	//	//	//	//	//	$0.6^{+0.2}_{-0.3}$

Note. Model parameters obtained by simultaneously fitting the 15 X-ray spectra of IC 751 (divided in five epochs). The table reports (1) the observation number, (2) the cloud column density, (3) the normalization of the primary power-law emission, (4) the photon index of the primary X-ray emission, (5) the equatorial column density of the torus, (6) the inclination angle of the observer (see Figure 3), (7) the normalization of the reflection component, (8) the temperature of the collisionally ionized plasma, and (9) the fraction of scattered unabsorbed emission. The upper part of the table refers to the MYTORUS model in his original formulation (with the addition of a cloud of neutral material; see Section 4.1), while the lower part reports the results obtained by using MYTORUS in the decoupled mode (Section 4.2). In the lower part column (5) is the torus column density of the MYTORUSZ component for $\theta_i(Z) = 90°$, and (6) is the column density of the MYTORUSS and MYTORUSL components, assuming $\theta_i(S, L) = 0°$ and $\theta_i(S, L) = 90°$.
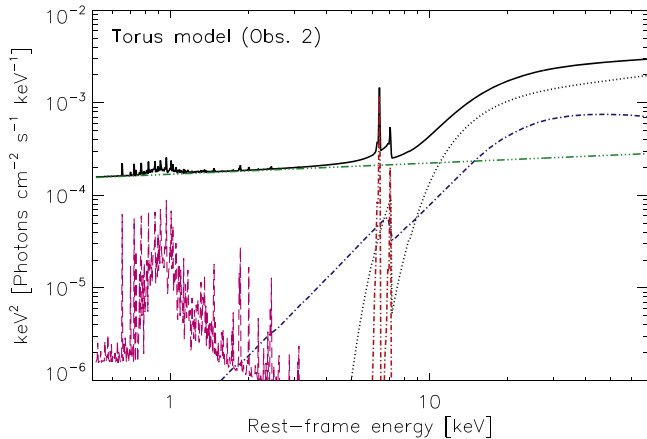
Figure 4. Torus spectral model used for the analysis of IC 751. The black continuous line represents the total flux, while the components shown are the absorbed X-ray power-law (ZPOW×ZTBABS×CABS×MYTORUSZ, dotted black line), the scattered component from the torus (MYTORUSS, dotted–dashed blue line), the fluorescent emission lines (MYTORUSL, dotted–dashed red line), the thermal component (magenta dashed line), and the scattered emission (green dotted–dotted–dashed line). The values are set to those obtained during Observation 2. For more details, see Section 4.1 and Table 3.

Figure 5. Historical X-ray variability of IC 751 in the 2–10 (top panel) and 10–50 keV (bottom panel) band. The filled and empty points represent the observed and intrinsic (i.e., corrected for absorption) fluxes, respectively. The red dashed line and the dotted–dotted–dashed green line represent the average observed and intrinsic fluxes, respectively.

The column density of the reprocessing material is found to be $N_H^T(S, L) = (6.0^{+3.5}_{-2.2}) \times 10^{24}$ cm^{-2}, while the line of sight non-variable absorber [$N_H^T(Z)$] has a lower value ($\sim 3.7 \times 10^{23}$ cm^{-2}) than that obtained considering a homogeneous torus (Section 4.1). The value of $N_H^T(Z)$ is consistent with the lowest value of N_H obtained by applying the slab model.

5. FLUX VARIABILITY AND TIME-RESOLVED SPECTROSCOPY

X-ray observations have shown that besides a highly variable line of sight column density, IC 751 also presents significant flux variability of the primary X-ray source on timescales of days to months both in the soft and hard X-ray bands (see Tables 2 and 3). As illustrated in Figure 5 (filled

points), the observed flux of IC 751 varies by a factor of 4 in the 2–10 keV band, and by a factor of 1.6 in the 10–50 keV band. When considering intrinsic fluxes (i.e., absorption-corrected, empty points in Figure 5), the amplitude of the variability is larger: the X-ray source varies by a factor of ~5 both in the 2–10 and 10–50 keV bands. The average observed fluxes in the 2–10 keV and 10–50 keV bands are 6.4×10^{-13} erg cm^{-2} s^{-1} and 4.0×10^{-12} erg cm^{-2} s^{-1}, respectively. The intrinsic average nuclear fluxes in the two bands are 7.4×10^{-12} erg cm^{-2} s^{-1} (2–10 keV) and 9.3×10^{-12} erg cm^{-2} s^{-1} (10–50 keV), which correspond to k-corrected average luminosities of $\log(L_{2-10}/$ erg s$^{-1})$ = 43.22 and $\log(L_{10-50}/$ erg s$^{-1})$ = 43.32. The 12 μm rest frame luminosity of IC 751 could be estimated using *WISE* by linearly interpolating the fluxes in the *W3* (11.56 μm) and *W4* (22.09 μm) bands. The mid-IR flux of IC 751 is dominated by the AGNs, since $W1 - W2 > 0.8$ (Stern et al. 2012). We found that the X-ray luminosity is in agreement with the 12 μm luminosity [$\log(L_{12\mu m}/$ erg s$^{-1})$ = 43.70], as expected from the well known mid-IR/X-ray correlation (e.g., Gandhi et al. 2009, Asmus et al. 2015, Stern 2015).

In order to improve our constraints on the absorbing material, and to study its evolution on shorter timescales, we analyzed the *XMM-Newton* EPIC/PN and *NuSTAR* light curves of IC 751 in different energy bands. We extracted *XMM-Newton* EPIC/PN light curves in the 0.3–10, 0.3–2, and 2–10 keV bands, with bins of 1 ks. *NuSTAR* FPMA light curves were extracted in the 3–79, 3–20, and 20–60 keV bands with bins of 6 ks. We also analyzed the variability of the hardness ratio, defined as $HR = H - S/H + S$, where H and S are the fluxes in the soft (0.3–2 and 3–20 keV) and hard (2–10 and 20–60 keV) bands, respectively.

For all the observations we performed a χ^2 test in order to assess the variability of the hardness ratio and the flux in the three different energy bands. We considered the flux or the hardness ratio to be variable if the minimum confidence level was $p \leqslant 1\%$. To constrain the amplitude of the variability, we used the rms variability amplitude ($F_{\rm var}$; see Equation (10) and B2 of Vaughan et al. 2003). *NuSTAR* light curves of Observation 2 show significant variability both in the broad and in the soft bands, while the other *NuSTAR* observations do not show any sign of short-term variability. The *XMM-Newton* light curve of Observation 5 shows significant flux variation in the hard band, while the flux is consistent with being constant during Observation 6. The largest value of the rms variability amplitude is found for the *NuSTAR* 3–20 keV light curve of Observation 2 ($F_{\rm var} = 34 \pm 7\%$). The hardness ratio is significantly variable only for the *NuSTAR* light curve of Observation 2 ($p \simeq 0.5\%$, $F_{\rm var} = 59 \pm 16\%$), which shows a hardening of the spectrum in the last ~6 ks of the observation.

The 104 month 14-195 *Swift*/BAT light curve does not show evidence of significant long-term variability ($p \sim 6\%$) on a timescale of 25 Ms.

We also carried out a time-resolved spectral analysis of the longest *NuSTAR* observation (Observation 3) by splitting it in five time intervals with similar lengths. We applied the slab model described in Section 3, leaving the normalization of the primary X-ray emission and the line of sight column density free to vary, and found that the parameters obtained are consistent within their 90% confidence interval between all observations. Leaving the value of $f_{\rm scatt}$ free to vary significantly improves the fit only for the second ($\Delta\chi^2 \simeq 8$) and third
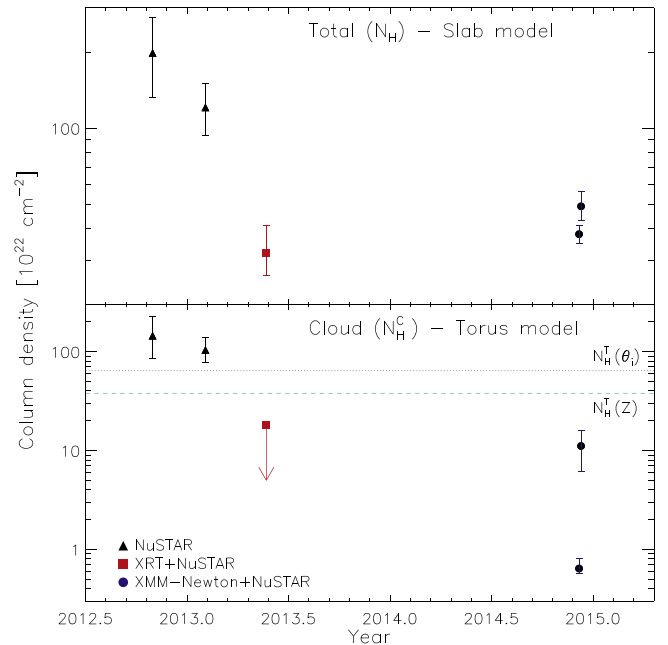
Figure 6. Column density variability of IC 751. Top panel: total line of sight column density ($N_{\rm H}$) obtained with the slab model described in Section 3. Bottom panel: column density of the varying absorber (cloud column density, $N_{\rm H}^{\rm C}$; see Figure 3) obtained with the torus spectral model discussed in Section 4. The black dotted line and the green dashed line represent the values of the non-variable column density of the torus obtained by using MYTORUS in its standard [$N_{\rm H}^{\rm T}(\theta_i)$] and decoupled [$N_{\rm H}^{\rm T}(Z)$] modes, respectively. The values of the line of sight column density are those obtained by using MYTORUS in the decoupled mode (Section 4.2).

($\Delta\chi^2 \simeq 7$) segments, and results in values consistent with those obtained for the other segments and for the whole observation.

6. DISCUSSION

The X-ray observations of IC 751 presented here show clear evidence of changes in the line of sight column density, with the X-ray source being obscured by Compton-thick [$\log(N_{\rm H}/$ cm$^{-2}) \sim 24.3$] material in two observations, and by Compton-thin material [$\log(N_{\rm H}/$ cm$^{-2}) \simeq 23.60$] in three observations. This result is confirmed adopting both the slab (Section 3, top panel of Figure 6) and the torus (Section 4, bottom panel of Figure 6) X-ray spectral models. In particular, by using a physical torus model, we were able, assuming a smooth and azimuthally symmetric torus, to disentangle the intrinsic obscuration associated with a non-varying absorber from the column density of the varying absorber. Variations in the observed line of sight column density might be related either to: (i) intrinsic variation of the absorbing material, caused by moving clouds; (ii) changes in the intensity of the nuclear radiation, which would cause a variation in the ionization state of the absorbing material. Although the observations during which the highest values of the column density were also found to correspond to the stage in which the source was more luminous, for a low-density photo-ionized absorber there might be delay between the flux variation and the response of the absorber, so that the second scenario cannot be completely discarded. In the following, we will, however, assume that changes in $N_{\rm H}$ are related to clouds eclipsing the X-ray source,

as found for several other changing look AGNs (e.g., Risaliti et al. 2005).

Following Risaliti et al. (2007) and Marinucci et al. (2013), the distance of the cloud from the X-ray source (R_c) can be estimated by considering that the size of the source and that of the cloud are similar ($D_c \simeq D_s$), and that the transverse velocity is given by the ratio between the size of the source (D_s) and the crossing time T_{cr}: $V_k = D_s/T_{cr}$. It must be remarked that in Observation 2 we found possible evidence of partial covering, which would imply that $D_c < D_s$. By applying the slab model, we found that the cloud covers 83% of the X-ray source. The value of the covering factor was larger when adopting the torus model ($\sim$96%). Given the rather large values of the covering factor, taking the possible difference between D_c and D_s into account does not significantly affect our results. Assuming that the cloud is moving with a Keplerian velocity, we obtain:

$$R_c = \frac{GM_{BH}}{V_k^2} = \frac{GM_{BH}T_{cr}^2}{D_s^2}. \qquad (2)$$

Micro-lensing (e.g., Chartas et al. 2002, 2009), occultation studies (Risaliti et al. 2009), and large-amplitude rapid X-ray variability have shown that the size of the X-ray source is $D_s \simeq 10\,r_g$, where $r_g = GM_{BH}/c^2$. Assuming that $D_s = 10\,r_g$, we obtain

$$R_c = \frac{GM_{BH}T_{cr}^2}{10^2 R_G^2} \simeq 2\text{ pc } M_{8.5}\,R_{10}^{-2}\,T_{10}^2, \qquad (3)$$

where T_{10} is the crossing time in units of 10 days (8.64×10^5 s) and $M_{8.5} = M_{BH}/10^{8.5}\,M_\odot$.

The black hole mass of IC 751 has recently been obtained by the study of the stellar velocity dispersion as part of work aimed at constraining the characteristics of *Swift*/BAT-selected AGNs in the optical band (M. J. Koss et al. 2016, in preparation), and is $\log(M_{BH}/M_\odot) \simeq 8.5$. By using Equation (3), and considering that (i) no significant variation was found during the 50 ks of *NuSTAR* Observation 3 (over a total of 100 ks), and that (ii) the shortest interval in which a variation of the CT material is evident is between Observation 3 and Observation 4, which were carried out 108 days apart, we can say that the distance of the cloud is between $R_{min} = 0.027$ pc ($\sim$32 light days) and $R_{max} \simeq 230$ pc.

Optical reverberation-mapping studies have shown that the radius of the BLR scales with the square root of the luminosity (e.g., Kaspi et al. 2005). According to Kaspi et al. (2005), considering the Hβ lags and the results obtained averaging different observations of the same object, the radius of the BLR is given by

$$\frac{R_{BLR}}{10\text{ lt} - \text{days}} = 0.86 \times \left(\frac{L_{2-10}}{10^{43}\text{ erg s}^{-1}}\right)^{0.532}. \qquad (4)$$

For the average 2–10 keV luminosity of IC 751, we find $R_{BLR} = 11.7$ light days, which implies that the obscuring clouds responsible for the variation of N_H are beyond the emission-weighted average radius of the BLR. Using a similar approach, it is possible to put constraints on the location of the hot inner wall of the torus, which is also known to scale with the square root of the luminosity (e.g., Suganuma et al. 2006, Kishimoto et al. 2011). Following Tristram & Schartmann 2011 (Figure 4 of their paper), the inner radius of the hot dust (R_{NIR}),

obtained from *K*-band reverberation, can be approximated by:

$$\log\frac{R_{NIR}}{1\text{ pc}} = -23.10 + 0.5\log L_{14-195}, \qquad (5)$$

where L_{14-195} is the 14–195 keV luminosity (in erg s^{-1}). At 12 μm, interferometric studies (Tristram & Schartmann 2011; see also Burtscher et al. 2013) have shown that the size of the mid-IR-emitting region (R_{MIR}) in AGNs can be estimated by

$$\log\frac{R_{MIR}}{1\text{ pc}} = -21.62 + 0.5\log L_{14-195}. \qquad (6)$$

The 70 month averaged 14–195 keV luminosity of IC 751 is $\log(L_{14-195}/\text{ergs}^{-1}) = 43.47$ (Baumgartner et al. 2013), which corresponds to $R_{NIR} = 0.04$ pc ($\sim$48 light days) and $R_{MIR} = 1.3$ pc. From this we can conclude that the absorbing material could be related to the outer BLR, to clumps in the molecular torus, or even to material located at a further distance from the SMBH.

A change in the Compton-thin absorber is also found between Observation 5 and Observation 6 using the slab spectral model and MyTORUS in its decoupled mode. The two observations were carried out about 48 hr apart, which means (applying Equation (3)) that for the Compton-thin material the $R \lesssim R_{max} = 0.08$ pc ($\sim$95 light days). If the Compton-thin and CT clouds are located at the same distance from the X-ray source, then the regions where the varying absorbers are located are between 32 and 95 light days. This would imply that the absorber is consistent with being located either in the BLR or in the inner side of the dusty torus. Recent work has shown that the Fe Kα might also arise in this region (Gandhi et al. 2015; Minezaki & Matsushita 2015). Assuming that the cloud has about the same size of the X-ray source, i.e., $\sim$10 r_g ($\sim$4.7 $\times$ 10^{14} cm), and that its column density is 1.5×10^{24} cm^{-2}, the density of the cloud would be $n \sim 3.2 \times 10^9$ cm^{-3}. This value is in agreement with that expected for the BLR clouds (e.g., Peterson 1997). A BLR origin for the varying absorber in IC 751 would fit what has been found so far for other changing look AGNs, several of which show absorbers compatible with being part of the BLR (e.g., Maiolino et al. 2010; Risaliti et al. 2010; Burtscher et al. 2015).

Thanks to its broadband coverage, *NuSTAR* is a very powerful tool to study obscuration in AGNs, and it has been shown to be fundamental to well constrain the line of sight column density (e.g., Arévalo et al. 2014; Bauer et al. 2015; Gandhi et al. 2014; Annuar et al. 2015; Koss et al. 2015; Lansbury et al. 2015). Studying type II quasars, Lansbury et al. (2015) have shown that the estimates of N_H obtained by *NuSTAR* can be 2.5–1600 times higher than previous constraints from *XMM-Newton* and *Chandra*. This shows that in the absence of high-quality broadband observations, it would be possible to miss changing look events for weak sources. Another clear example is given by the recent detection of an unveiling event in NGC 1068 (Marinucci et al. 2016), which would have been missed by observations carried out below 10 keV. Repeated *NuSTAR* observations of obscured sources might therefore uncover a significant number of new changing look events. Burtscher et al. (2015) have recently reanalyzed the relation between N_H and the optical obscuration A_V, and found that in several cases the deviation of N_H/A_V from the Galactic value is due to variable absorption. This

would imply that ideal targets to study occultations of the X-ray source are objects showing a large deviation from the Galactic N_H/A_V value.

7. SUMMARY AND CONCLUSIONS

We reported here on the spectral analysis of five *NuSTAR* observations of the type 2 AGN IC 751, three of which were combined with *XMM-Newton* or *Swift*/XRT observations in the 0.3–10 keV range. IC 751 is the first changing look AGN (i.e., an object that has been observed both in a Compton-thin and a CT state) discovered by *NuSTAR*. We find that the X-ray source was obscured by CT material during the first two observations, while its line of sight obscuration is found to be Compton-thin during the following observations, which implies that absorption varies on timescales of $\lesssim 3$ months. Changes of the line of sight column density are also found on a timescale of ~ 48 hr ($\Delta N_H \sim 10^{23}$ cm^{-2}). While we cannot constrain the location of the absorber precisely, by considering the lack of spectral variability during the longest *NuSTAR* observation we can infer the minimum distance to be further than the emission-weighted average radius of the BLR. Assuming that the varying Compton-thin and CT clouds are located at the same distance from the X-ray source, then the material is located between 32 and 95 light days. The absorber could therefore be related to either the external part of the BLR or to the inner part of the dusty torus, although the BLR origin might be slightly favored since the density of the clouds is found to be consistent with the value expected for BLR clouds. By adopting a physical torus X-ray spectral model, we are able to disentangle the column density of the non-varying absorber ($N_H \sim 3.8 \times 10^{23}$ cm^{-2}) from that of the varying clouds [$N_H \sim (1\text{–}150) \times 10^{22}$ cm^{-2}], and to put constraints on the column density of the reprocessing material ($N_H \sim 6 \times 10^{24}$ cm^{-2}). We found that the X-ray source is highly variable in both the 2–10 keV and 10–50 keV bands. Future observational campaigns on IC 751 in the X-ray band will be able to improve the constraints on the location of the varying absorber, and confirm or not whether it is related to clouds in the BLR as has been found for several objects of this class.

REFERENCES

Annuar, A., Gandhi, P., Alexander, D. M., et al. 2015, ApJ, 815, 36
Arévalo, P., Bauer, F. E., Puccetti, S., et al. 2014, ApJ, 791, 81
Arnaud, K. A. 1996, in ASP Conf. Ser. 101, Astronomical Data Analysis Software and Systems V, ed. G. H. Jacoby, & J. Barnes (San Francisco, CA: ASP), 17
Asmus, D., Gandhi, P., Hoenig, S. F., Smette, A., & Duschl, W. J. 2015, MNRAS, 454, 766
Bauer, F. E., Arevalo, P., Walton, D. J., et al. 2015, ApJ, 812, 116
Baumgartner, W. H., Tueller, J., Markwardt, C. B., et al. 2013, ApJS, 207, 19
Beckmann, V., Jean, P., Lubiński, P., Soldi, S., & Terrier, R. 2011, A&A, 531, A70
Bianchi, S., Guainazzi, M., Matt, G., et al. 2005, A&A, 442, 185
Bianchi, S., Maiolino, R., & Risaliti, G. 2012, AdAst, 2012, 17
Bianchi, S., Piconcelli, E., Chiaberge, M., et al. 2009, ApJ, 695, 781
Braito, V., Ballo, L., Reeves, J. N., et al. 2013, MNRAS, 428, 2516
Burrows, D. N., Hill, J. E., Nousek, J. A., et al. 2005, SSRv, 120, 165
Burtscher, L., Davies, R. I., Gracia-Carpio, J., et al. 2015, A&A, 586, 28
Burtscher, L., Meisenheimer, K., Tristram, K. R. W., et al. 2013, A&A, 558, A149
Cash, W. 1979, ApJ, 228, 939
Chartas, G., Agol, E., Eracleous, M., et al. 2002, ApJ, 568, 509
Chartas, G., Kochanek, C. S., Dai, X., Poindexter, S., & Garmire, G. 2009, ApJ, 693, 174
de Vaucouleurs, G., de Vaucouleurs, A., Corwin, H. G., Jr., et al. 1991, S&T, 82Q, 621
Elvis, M., Risaliti, G., Nicastro, F., et al. 2004, ApJL, 615, L25
Falco, E. E., Kurtz, M. J., Geller, M. J., et al. 1999, PASP, 111, 438
Gabriel, C., Denby, M., Fyfe, D. J., et al. 2004, in ASP Conf. Ser. 314, Astronomical Data Analysis Software and Systems (ADASS) XIII, ed. F. Ochsenbein, M. G. Allen, & D. Egret (San Francisco, CA: ASP), 759
Gallagher, S. C., Brandt, W. N., Wills, B. J., et al. 2004, ApJ, 603, 425
Gandhi, P., Hoenig, S. F., & Kishimoto, M. 2015, ApJ, 812, 113
Gandhi, P., Horst, H., Smette, A., et al. 2009, A&A, 502, 457
Gandhi, P., Lansbury, G. B., Alexander, D. M., et al. 2014, ApJ, 792, 117
Gehrels, N., Chincarini, G., Giommi, P., et al. 2004, ApJ, 611, 1005
Guainazzi, M. 2002, MNRAS, 329, L13
Guainazzi, M., Matt, G., Fiore, F., & Perola, G. C. 2002, A&A, 388, 787
Harrison, F. A., Craig, W. W., Christensen, F. E., et al. 2013, ApJ, 770, 103
Immler, S., Brandt, W. N., Vignali, C., et al. 2003, AJ, 126, 153
Jansen, F., Lumb, D., Altieri, B., et al. 2001, A&A, 365, L1
Kalberla, P. M. W., Burton, W. B., Hartmann, D., et al. 2005, A&A, 440, 775
Kaspi, S., Maoz, D., Netzer, H., et al. 2005, ApJ, 629, 61
Kishimoto, M., Hönig, S. F., Antonucci, R., et al. 2011, A&A, 527, A121
Koss, M. J., Romero-Canizales, C., Baronchelli, L., et al. 2015, ApJ, 807, 149
LaMassa, S. M., Cales, S., Moran, E. C., et al. 2015, ApJ, 800, 144
Lamer, G., Uttley, P., & McHardy, I. M. 2003, MNRAS, 342, L41
Lansbury, G. B., Gandhi, P., Alexander, D. M., et al. 2015, ApJ, 809, 115
Longinotti, A. L., Bianchi, S., Ballo, L., de La Calle, I., & Guainazzi, M. 2009, MNRAS, 394, L1
Madsen, K. K., Harrison, F. A., Markwardt, C., et al. 2015, ApJS, 220, 8
Magdziarz, P., & Zdziarski, A. A. 1995, MNRAS, 273, 837
Maiolino, R., Risaliti, G., Salvati, M., et al. 2010, A&A, 517, A47
Marchese, E., Braito, V., Della Ceca, R., Caccianiga, A., & Severgnini, P. 2012, MNRAS, 421, 1803
Marinucci, A., Bianchi, S., Matt, G., et al. 2016, MNRAS, 456, L94
Marinucci, A., Risaliti, G., Wang, J., et al. 2013, MNRAS, 429, 2581
Markowitz, A. G., Krumpe, M., & Nikutta, R. 2014, MNRAS, 439, 1403
Matt, G., Guainazzi, M., & Maiolino, R. 2003, MNRAS, 342, 422
Minezaki, T., & Matsushita, K. 2015, ApJ, 802, 98
Miniutti, G., Sanfrutos, M., Beuchert, T., et al. 2014, MNRAS, 437, 1776
Murphy, K. D., & Yaqoob, T. 2009, MNRAS, 397, 1549
Nardini, E., & Risaliti, G. 2011, MNRAS, 417, 2571
Peterson, B. M. 1997, An Introduction to Active Galactic Nuclei (iagn.book)
Piconcelli, E., Bianchi, S., Guainazzi, M., Fiore, F., & Chiaberge, M. 2007, A&A, 466, 855
Pounds, K. A., Reeves, J. N., Page, K. L., & O'Brien, P. T. 2004, ApJ, 616, 696
Puccetti, S., Fiore, F., Risaliti, G., et al. 2007, MNRAS, 377, 607
Ricci, C., Ueda, Y., Ichikawa, K., et al. 2014a, A&A, 567, A142

Ricci, C., Ueda, Y., Koss, M. J., et al. 2015, ApJL, 815, L13
Ricci, C., Ueda, Y., Paltani, S., et al. 2014b, MNRAS, 441, 3622
Risaliti, G., Elvis, M., Bianchi, S., & Matt, G. 2010, MNRAS, 406, L20
Risaliti, G., Elvis, M., Fabbiano, G., Baldi, A., & Zezas, A. 2005, ApJL, 623, L93
Risaliti, G., Elvis, M., Fabbiano, G., et al. 2007, ApJL, 659, L111
Risaliti, G., Elvis, M., & Nicastro, F. 2002, ApJ, 571, 234
Risaliti, G., Nardini, E., Salvati, M., et al. 2011, MNRAS, 410, 1027
Risaliti, G., Salvati, M., Elvis, M., et al. 2009, MNRAS, 393, L1
Rivers, E., Baloković, M., Arévalo, P., et al. 2015a, ApJ, 815, 55
Rivers, E., Markowitz, A., & Rothschild, R. 2011, ApJL, 742, L29
Rivers, E., Risaliti, G., Walton, D. J., et al. 2015b, ApJ, 804, 107
Sanfrutos, M., Miniutti, G., Agís-González, B., et al. 2013, MNRAS, 436, 1588
Shappee, B. J., Prieto, J. L., Grupe, D., et al. 2014, ApJ, 788, 48

Shu, X. W., Yaqoob, T., & Wang, J. X. 2010, ApJS, 187, 581
Stern, D. 2015, ApJ, 807, 129
Stern, D., Assef, R. J., Benford, D. J., et al. 2012, ApJ, 753, 30
Strüder, L., Briel, U., Dennerl, K., et al. 2001, A&A, 365, L18
Suganuma, M., Yoshii, Y., Kobayashi, Y., et al. 2006, ApJ, 639, 46
Torricelli-Ciamponi, G., Pietrini, P., Risaliti, G., & Salvati, M. 2014, MNRAS, 442, 2116
Tristram, K. R. W., & Schartmann, M. 2011, A&A, 531, A99
Turner, M. J. L., Abbey, A., Arnaud, M., et al. 2001, A&A, 365, L27
Vaughan, S., Edelson, R., Warwick, R. S., & Uttley, P. 2003, MNRAS, 345, 1271
Véron-Cetty, M.-P., & Véron, P. 2010, A&A, 518, A10
Walton, D. J., Risaliti, G., Harrison, F. A., et al. 2014, ApJ, 788, 76
Wilms, J., Allen, A., & McCray, R. 2000, ApJ, 542, 914
Yaqoob, T. 2012, MNRAS, 423, 3360